

Characterization of viscoelastic properties of asphalt mixture at low temperatures using DC(T) creep test



Behnam Jahangiri^{a,*}, Mohammad M. Karimi^b, Oliver Giraldo-Londoño^c, William G. Buttlar^d

^a Lyles School of Civil Engineering, Purdue University, United States

^b Civil and Environmental Engineering Department, Tarbiat Modares University, Iran

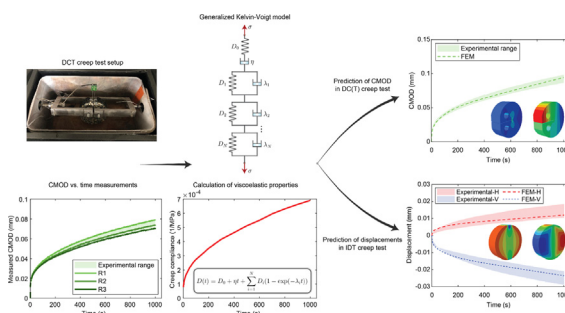
^c Civil and Environmental Engineering Department, University of Missouri-Columbia, United States

^d Glen Barton Chair in Flexible Pavements, Civil and Environmental Engineering Department, University of Missouri-Columbia, United States

HIGHLIGHTS

- DC(T) and IDT creep tests were conducted at low-temperatures and compared.
- A DC(T) geometry coefficient was determined via 3D finite element analysis.
- Viscoelastic models were fit to results obtained from the DC(T) creep test.
- Numerical simulations were validated against DC(T) and IDT creep experiments.

GRAPHICAL ABSTRACT



ARTICLE INFO

Article history:

Received 8 November 2020

Received in revised form 8 May 2021

Accepted 22 May 2021

Keywords:

Asphalt concrete
DC(T) creep test
Viscoelasticity
Low temperature
Numerical simulation

ABSTRACT

This study presents a framework to identify the low-temperature viscoelastic properties of asphalt concrete using the disk-shaped compacted tension (DC(T)) creep test. Due to the DC(T) geometry, the stress-strain state in the DC(T) geometry is not simple, and a geometry coefficient is needed to characterize the relationship between the mechanical and geometrical properties. The geometry coefficient of DC(T) was calculated by invoking the correspondence principle in viscoelasticity. The DC(T) creep test was conducted on different asphalt mixtures comprised of various components and modifiers at three temperature levels of 0, -12, and -24 °C. The creep compliance function for each of these mixtures was modeled using a generalized Voigt-Kelvin spring-dashpot phenomenological representation. The numerical implementation of the generalized Voigt-Kelvin model was developed in the finite element code Abaqus via a user material subroutine (UMAT). Numerical simulations of DC(T) creep tests using the identified viscoelastic properties are presented, which indicate the capability of the proposed approach to characterize the low-temperature linear viscoelastic behavior of the investigated asphalt mixtures. To further validate the viscoelastic properties obtained from DC(T) test through different stress-strain states, numerical simulation results from an Indirect Tensile Creep Test were compared to experimental results. The close agreement found between the results of indirect tensile creep tests and numerical simulations indicates the capability of the proposed approach for identification of viscoelastic properties of asphalt mixtures at low temperatures, which opens the door to avoid the intricate experimental setup and poor repeatability of the indirect tensile creep test at low temperatures.

© 2021 Elsevier Ltd. All rights reserved.

* Corresponding author at: Lyles School of Civil Engineering, Purdue University, United States.

E-mail addresses: bjahangiri@purdue.edu (B. Jahangiri), mohammad.karimi@modares.ac.ir (M.M. Karimi), ogiraldo@missouri.edu (O. Giraldo-Londoño), buttlar@missouri.edu (W.G. Buttlar).

1. Introduction

Asphalt concrete suffers from low temperature cracking in cold regions. This type of pavement distress occurs due to the stress built-up in the pavement structure under temperature fluctuation. To calculate the thermally induced stress, viscoelastic characteristics of the asphalt mixture need to be characterized. Creep compliance provides a simple measure of the linear viscoelastic nature of asphalt concrete at low temperatures, and is often employed in thermal cracking models and can be used to evaluate the ability of the asphalt concrete to relax thermal stresses in response to rapid cooling events in the field [1]. This material property can be characterized using experimental data from a creep test conducted by applying a rapidly applied, 'step-stress', which is then held constant as the time-dependent creep displacement is measured [2]. Various thermal cracking prediction models (e.g. TCMODEL [3,4] and ILLI-TC [5,6]) use viscoelastic creep compliance as a key input to the models, mainly for response calculation. In some cases, parameters derived from the creep compliance curve are also used in cracking models, such as measures of the slope of the creep compliance curve at long loading times [3,4], which is often called the 'm-value.'

1.1. Overview: Available creep test set-ups

Researchers have proposed different test setups, such as uniaxial cylindrical [7,8], semi-circular bending (SCB) [9], thermal stress restrained specimen test (TSRST) [10,11], indirect tension (IDT) [12,13], and bending beam geometries [14,15] to determine the creep compliance of asphalt mixtures. The uniaxial test can be performed in either pure tension or pure compression modes. Moreover, the stress level in the uniaxial test is constant throughout the cylindrical sample, providing a straightforward creep compliance calculation method. However, the uniaxial test requires testing specimens that cannot be fabricated from field cores due to the limited thickness of the asphalt lifts in a pavement structure. On the other hand, the SCB-type configuration benefits from a simple specimen fabrication process and can be performed on field cores as well. However, the bending moment (flexural stress) within the SCB sample is assumed to result in non-linear behavior and damaging of the sample. Besides, most of the available tests performed on the SCB configuration are performed at room temperature (25 °C) and, therefore, do not need a temperature-control chamber. Due to the highly temperature dependent behavior of asphalt mixtures and the duration of the creep test (100–1000 s), the testing temperature needs to be controlled and maintained throughout the experiment. As a result, the uniaxial and SCB creep tests are not suitable for a considerable amount of applications in research and industry. In the following sections, the frequently applied creep tests including IDT and bending beam rheometer (BBR) tests are reviewed. In order to investigate the thermal stress buildup in asphalt pavements during cooling events, a constant cooling rate is applied in TSRST set-up [16]. Further, Velásquez et al. [17] provided a method to address the issue associated with the rotation of the platens due to poor specimen alignment and material heterogeneity in the TSRST test.

1.2. Indirect tension (IDT) type creep compliance

Following AASHTO T322-2007, the Superpave IDT test can be used to measure the creep compliance and strength of asphalt concrete. The field-cored or gyratory-compacted samples with heights ranging from 38 to 50 mm and diameters in the range of 150 ±9 mm are generally used. Three testing temperatures with 10 °C intervals are recommended, which are often taken as 0, –10, and

–20 °C. Alternatively, temperatures can be selected to encompass the low-performance grade (PG) of the asphalt binder and can use a different temperature spacing, such as 0, –12, and –24 °C [6]. A creep test duration of 1000 s is generally required to ensure overlap between creep curves for master curve development. Since the creep compliance should normally be characterized in the linear viscoelastic range, loading levels should be kept sufficiently low to retain this linearity. Therefore, a maximum deformation on the horizontal clip gage of 0.019 mm for 150 mm diameter samples is suggested to stay within the linear range. Besides, to circumvent the noise problems and drift inherent in sensors (displacement extensometers), a minimum deformation of 0.00125 mm at a 30-second loading time is recommended [12]. The IDT test setup and loading configurations pose both tensile and compressive stresses in both horizontal and vertical directions. Therefore, the stress and strain states in the IDT test are not as simple as those in uniaxial loading. Due to this complexity, a geometrical coefficient (or creep compliance correction factor) is calculated using the horizontal and vertical deflection and is applied in the creep compliance formula per AASHTO T322.

The IDT test has been the most frequently applied test by researchers and agencies to calculate the creep compliance at low temperatures and evaluate the cracking potential of asphalt mixtures [18–21]. For example, Behnia et al. [22] fitted a power law function on IDT creep compliance master curves to characterize low temperature behavior of four mixtures with PG 64–22 and PG 58–28 binder types containing 20 and 40% reclaimed asphalt pavement (RAP). Dave et al. [5] introduced the ILLI-TC software, which simulates low temperature cracking in asphalt pavements using a 2D viscoelastic finite element (FE) analysis with cohesive zone fracture modeling. Hill et al. [23] used bio-based modifiers to improve the thermal cracking resistance of recycled mixtures. To this end, DC(T) fracture and IDT bulk viscoelastic characterization tests were used. The m-value increases as the bio-based modifier is added to hot mix asphalt (HMA). Moreover, the addition of RAP resulted in a significant reduction in m-value. To numerically study the effect of material heterogeneity on the fracture of asphalt concrete, Wills et al. [24] performed IDT creep tests on mixtures containing different air void contents and found that higher air voids lead to higher compliance in asphalt mixtures.

1.3. Bending beam rheometer (BBR) type creep compliance

The creep compliance of the asphalt mixtures obtained from the BBR test involves three-point loading of the asphalt samples fabricated in the form of a beam with standard dimensions of 115 × 12.7 × 6.35 mm (length × width × thickness) per AASHTO TP 125. Normally, three testing temperatures are chosen for this test. Test temperatures equal to 4, 10, and 16 °C above the low performance grade (PG) of the binder used in the mix have been successfully employed. The testing specimens could be obtained from both gyratory compacted and field core samples. Fifteen to twenty BBR specimens can be fabricated out of each gyratory sample and a minimum of five replicates is recommended by the standard for each temperature. A loading level of 4000 mN is applied on the beam specimen for 240 s. The viscoelastic properties of the asphalt mixture are calculated using the deflection measured in time.

Zofka et al. [14] tested 20 different mixture types consisting of 10 binder types and 2 aggregate sources. The BBR apparatus was utilized to obtain creep compliance of thin asphalt mixture specimens. Due to the small cross sectional dimensions of BBR specimens (12.7 mm by 6.35 mm), the representative volume element (RVE), which accounts for reliability and repeatability to set the minimum dimensions of the testing sample, was not met [14]. The maximum aggregate size is often larger than the specimen width, and much larger than the specimen thickness. Nevertheless,

due to the averaging effect along the relatively long beam, the BBR and the reference IDT creep compliance values were found to be in reasonable agreement [25]. Also, using measured IDT creep compliance and predicted IDT creep compliance from BBR creep data, it was shown that similar crack depths and amount of cracking were predicted by TCMODEL [25]. The BBR mixture test is especially attractive for characterizing near-surface asphalt mixture creep properties, where high property gradients exist [26]. The AASHTO TP 125 procedure has been used by researchers to investigate the effect of aging on low temperature cracking potential and also to find the equivalent aging time between the loose mixture and gyratory compacted specimen aging protocols [27–30]. Recently, Judycki [31] implemented analytical solution to develop a new viscoelastic method integrated with Burger's model to calculate the thermally induced stress. The viscoelastic properties of this solution have been calibrated through a creep test on $300 \times 50 \times 50$ mm asphalt beam samples with a constant loading level ranging from 20 to 35% of the bending strength for 2400 s followed by 1200 s of resting period [16].

1.4. Introducing disk-shaped compact tension (DC(T)) test

The DC(T) fracture test was introduced by Wagoner et al. in 2005 [32] to investigate the fracture resistance of the asphalt mixtures. One of the main advantages of the DC(T) geometry compared to the available SCB-type fracture tests is its larger ligament length such that the ratio between the average aggregate size and the fracture area is low. In other words, the number of aggregates acting as obstacles to crack propagation is high. This allows the complete release of fracture energy, and credits the role of aggregates [33]. The DC(T) test set-up benefits from a robust cooling chamber and uses a crack mouth opening displacement (CMOD) system to control the deflection at the top of a notched specimen [34]. The DC(T) fracture test has been used by various researchers and agencies during the last decade and is found to establish a good correlation with the pavement thermal cracking potential [35–37]. The DC(T) test has also been used for mixture characterization and to investigate the effect of the mix constituents on the low temperature cracking resistance [38–41].

The IDT test set-up requires an expensive loading frame and cooling chamber, which limits its practical use in routine mixture design and evaluation. In addition, the extensometers used to measure the vertical and horizontal deflections in the IDT test are costly and need continuous maintenance and calibration. The BBR test tries to avoid this issue as the test is performed in a Superpave binder BBR test, which is relatively more available in asphalt labs. However, there is concern whether or not the thin beam specimens can properly represent the properties of asphalt mixture, due to size effect concerns, as the dimensions of the aggregates used in asphalt concrete are generally larger than the thickness of the BBR specimen. In this research, to address the difficulties and uncertainties associated with the IDT and BBR mixture creep tests, the DC(T) geometry is employed as a practical alternative. Although typically used to evaluate asphalt mixture fracture resistance, the DC(T) test is employed herein, where one of the industry standard test devices was upgraded to permit creep testing.

1.5. Scope and objectives

- Calculating a geometrical coefficient for the DC(T) test which allows for a simple calculation of viscoelastic creep compliance from data streams collected from the industry standard DC(T) test device;

- Characterizing the viscoelastic behavior of asphalt mixtures at low temperatures using CMOD versus time results at low temperatures, along with creep load and the new geometrical coefficient and comparing results to the well established Superpave indirect tension test (IDT);
- Conducting test simulations using the finite element method (FEM) to predict the viscoelastic response and to validate the new geometrical coefficient.

To fulfill these objectives, a step-by-step approach was followed, as shown in Fig. 1.

2. Materials, sample fabrication, and test setup

In the experimental portion of this study, six stone-matrix asphalt (SMA) type mixtures were produced and used to fabricate testing samples for the DC(T) and IDT creep tests. The selected plant-produced asphalt mixtures were sampled per AASHTO T-168-03 across asphalt plants in the Chicago Area. Mixtures were sampled into uncoated, 5-gallon steel pails with tight-fitting lids. A representative from the Missouri Asphalt Pavement and Innovation Lab (MAPIL). After fabrication of the testing samples, the DC(T) and IDT test set-ups were used to conduct static creep tests (constant load) of 1000 s duration, where viscoelastic deflections were measured as a function of time. More details regarding data collection and analysis are provided later in this paper.

2.1. Materials

Table 1 presents the compositional properties of the mixtures used in this study. The first four mixtures (labeled as 1844, 1835, 1824, and 1845) are friction-surface-type SMAs, used on highway curves and ramps, while the last two SMA mixtures (1836 and 1840) are regular SMA surface mixtures, used in lower trafficked, non-curved or tangent road alignments. Among these mixtures, three of them (1844, 1824, and 1836) involved SBS-polymer-modified binder systems and the other three (1835, 1845, and 1840) involved ground tire rubber (GTR), modified either by a terminal-blend, wet process or by the so-called dry process. The 1835 mix utilized a relatively soft, neat binder (Superpave PG 46–34) combined with 10% engineered crumb rubber (ECR) by weight of binder (a dry-process GTR system). This mix also had the highest amount of recycled materials among all of the SMAs investigated (41.2% asphalt binder replacement [ABR]), including 25.1% ABR by RAP and 16.1% ABR by recycled roofing shingles (RAS). Similar to 1835, the 1845 mix was also made of PG 46–34 neat binder, which was later modified by 10.5% rubber by weight of the binder. The neat binder used in the 1840 mix was PG 58–28. The binder in this mix possessed 12.0% GTR, added to the binder via a terminal-blend, wet process. Aggregate gradations for all mixtures are shown in Fig. 2. It can be seen that the gradation of all SMAs investigated is quite similar, all with a nominal maximum aggregate size (NMAS) of 12.5 mm.

2.2. Sample fabrication

The sampled plant-produced mixtures were brought back to the MAPIL facility in 5-gallon steel pails. The plastic handles were removed and then pails were placed in a forced draft oven to heat the asphalt mixture to a workable consistency (~ 100 °C). The heated mixture was then reduced to the mass of the gyratory sample following the quartering method in AASHTO R47 (see Fig. 3). A Pine GB2 Superpave gyratory compactor was used to compact the reheated samples and make cylindrical specimens. After splitting

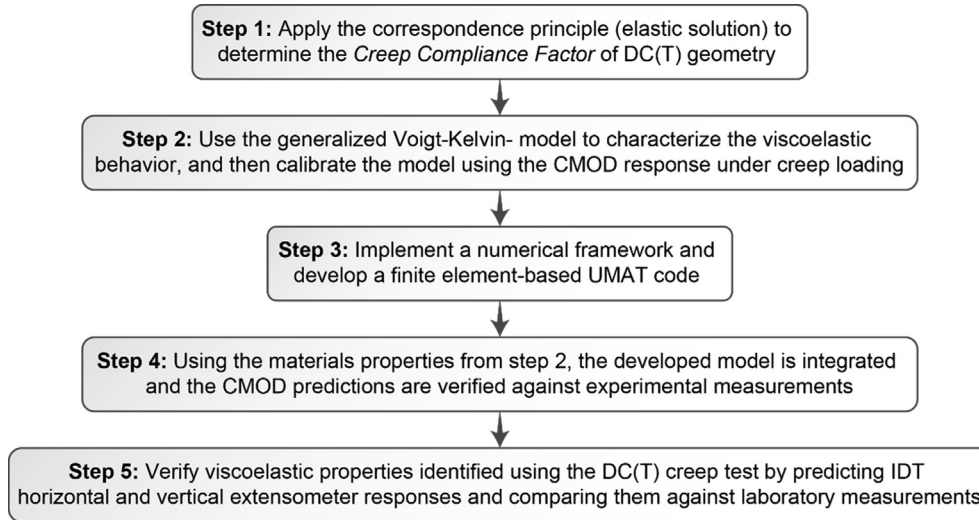


Fig. 1. Study Framework.

Table 1
Details of mixture ingredients.

Mix. ID	SMA ¹ Type	Base Binder	Total Binder Content (%)	ABR ² by RAP ³ (%)	ABR by RAS ⁴ (%)	NMAS ⁵ (mm)
1844	Friction Surface	SBS 70–28	6.12	10.8	16.0	12.5
1835	Friction Surface	46–34 + 10%ECR	5.93	25.1	16.1	12.5
1824	Friction Surface	SBS 64–34	6.14	20.4	16.7	12.5
1845	Friction Surface	46–34 + 10.5%GTR	6.21	23.9	15.4	12.5
1836	Surface	SBS 64–34	6.03	16.2	16.3	12.5
1840	Surface	58–28 + 12%GTR	6.03	15.9	9.8	12.5

1-SMA: Stone Matrix Asphalt; 2-ABR: Asphalt Binder Replacement; 3- RAP: Reclaimed Asphalt Pavement; 4- Recycled Roofing Shingles; 5- NMAS: Nominal Maximum Aggregate Size

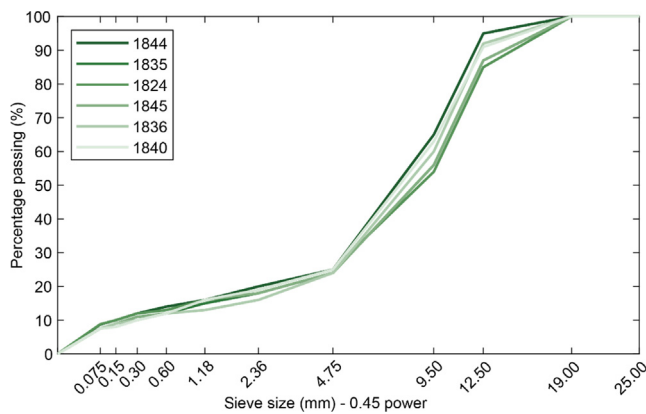


Fig. 2. Aggregate gradations for the investigated plant-produced mixtures.



Fig. 3. Splitting the bucket of mixture as per AASHTO R47.

to the desired mass, the asphalt mixture was heated to compaction temperature (155 and 143 °C for modified and unmodified mixes, respectively). All SMA testing samples were compacted to 6.0% air voids. For DC(T) samples, air voids were measured on the 50 mm slices before notching and coring for the DC(T) specimens.

2.3. DC(T) creep test set-up

DC(T) specimens were fabricated as per ASTM D7313 with a diameter of 150 mm, thickness of 50 mm and ligament length of 84.5 mm, along with two loading holes, each 25 mm in diameter.

The dimensions of each DC(T) sample, including thickness, diameter, and ligament length were measured, recorded, and then CMOD gage points were glued to the crack mouth of the specimen. The specimen was then placed into the DC(T) chamber for conditioning at the testing temperature for a minimum of 2 h and a maximum of 4 h. Next, samples were suspended from the cylindrical loading fixtures. To avoid damaging the samples, creep loading levels as low as 0.3, 0.4, and 0.5 kN were chosen for the testing temperatures of 0, -12, and -24 °C, respectively. These levels were determined after a non-trivial, trial-and-error process. Choosing an overly low load level is undesirable, as it will lead to noises in deflection

measurements; whereas selecting an overly high creep load leads to nonlinear behavior, either localized damage or crack initiation and propagation at the crack tip. Prior to the application of the creep test load, a seating load of 0.1 kN was applied to the sample. The aim of the seating load is to ensure that the sample had been engaged by the loading platens, and to minimize movement of the sample when the main creep load is applied. Fig. 4 shows the DC(T) test sample, test device, and an example of CMOD versus time under creep loading for three replicates of one mixture type. As seen in Fig. 4, three replicates were conducted on each mixture type. Table 2 presents the loading details of the DC(T) creep test at each temperature.

3. Analysis of experimental results

3.1. Determining the creep compliance factor

The viscoelastic properties of asphalt concrete are often experimentally determined using a uniaxially-loaded, cylindrical specimen because of the simple and straightforward stress-strain relationship. The stress level under uniaxial loading σ is assumed constant at every point throughout the sample and is simply calculated as the load level divided by the cross-sectional area. The strain is simply calculated as the ratio of displacement measured by the loading machine divided by the original height of the specimen, or by using simple, surface-mounted displacement sensors (ASTM D-3497). However, a more complex, three-dimensional geometry exists in the DC(T) test, which leads to much more complex stress-strain states in the specimen, especially considering the added complexity associated with the time-dependent (viscoelastic) behavior of bituminous materials. The correspondence principle provides a powerful tool for the analysis of viscoelastic boundary value problems (BVPs) for homogeneous and non-homogenous materials [42,43]. Using the correspondence principle, the 3-D viscoelastic solutions can be developed based on the elastic solution [44,45]. To this end, first, an elastic solution for a given specimen geometry is obtained as a function of applied load, geometry, and elasticity properties. Then, the viscoelastic solution of the investigated sample geometry is produced in accordance with the correspondence principle, where viscoelastic constitutive models are substituted in place of the elastic constants.

Considering the dimension compatibility in continuum mechanics, the relationship between the applied load, P , the specimen thickness, B , elasticity modulus, E , and crack mouth opening displacement (CMOD) is assumed as follows:

$$CMOD = \alpha \frac{P}{E \times B} \tag{1}$$

where α is the geometry coefficient, depending on the geometrical configuration of the ASTM D7313-17 DC(T) specimen. As shown in Eq. (1), the geometry coefficient completes the relationship between the mechanical and geometrical features of the DC(T) specimen. To calculate the geometry coefficient, the CMOD for various values of elasticity modulus, sample thickness, and the load was calculated using the finite element method and applied to the elastic solution. Then, considering Eq. (1) and results obtained from the elastic solution, the geometry coefficient was back calculated from simulation results as $\alpha = 25.0$. Therefore, Eq. (1) can be re-written as follows.

$$D = \frac{1}{E} = 0.04 \frac{B}{P} CMOD \tag{2}$$

where D is the inverse of the elastic modulus and is referred to as elastic compliance.

According to the definition of viscoelastic creep compliance (i.e., $\epsilon(t) = \sigma_0 D(t)$; ϵ : strain; σ_0 : constant stress), for the case of constant applied load, the viscoelastic solution and then the viscoelastic creep compliance for the DC(T) geometry was determined as follows:

$$D(t) = 0.04 \frac{B}{P_0} CMOD(t) \tag{3}$$

where $D(t)$ is the viscoelastic creep compliance and P_0 is the constant applied load in the DC(T) test.

Moreover, for the case of time-dependent applied load, the viscoelastic solution can be defined in accordance with Boltzmann (hereditary) integral, such that:

$$CMOD(t) = \frac{1}{0.04B} \left[D(t)P(0) + \int_{0^+}^t D(t - \tau) \frac{\partial P(\tau)}{\partial \tau} d\tau \right] \tag{4}$$

where $P(t)$ is the time-dependent applied load in the DC(T) test.

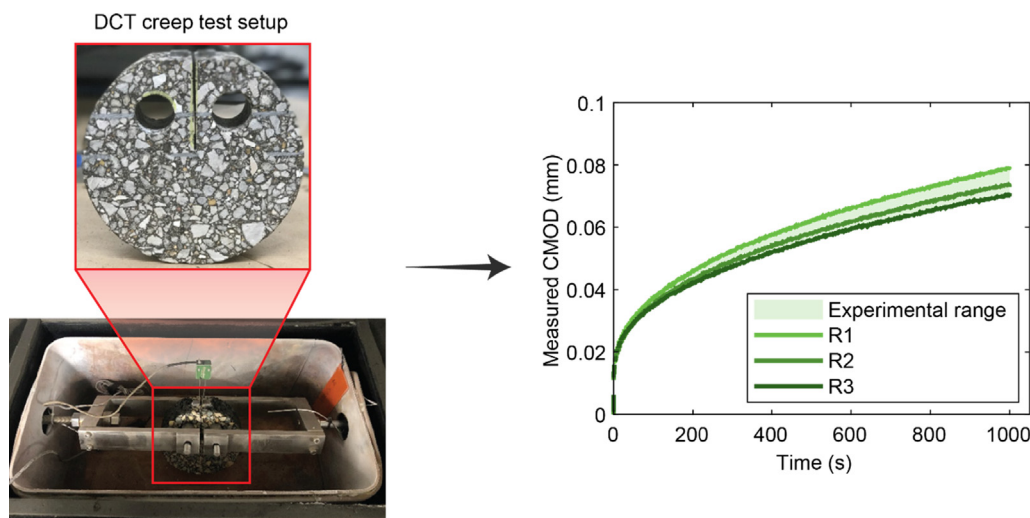


Fig. 4. A sample of the test output from DC(T) machine: three replicates (R1, R2, and R3) were tested for each temperature.

Table 2
Loading properties in DC(T) creep test.

Test	Testing Temp. (°C)	Chamber Temp. (°C)	Seating Load (kN)	Ramp Time (s)	Creep Load (kN)	Creep Time (s)
DC(T) creep	0	0	0.1	0.1	0.3	1000
	-12	-12			0.4	
	-24	-24			0.5	

3.2. Identification of viscoelastic properties

In this research, the DC(T) creep tests were conducted at three temperatures under a constant load applied for 1000 s, as shown in Table 2. The CMOD measurements collected at every 0.1 s are implemented to calculate the creep compliance according to Eq. (3). Three replicates were used for each mix type and the average creep compliance used in the subsequent analysis. The generalized Voigt-Kelvin model is then used to describe the elastic and viscoelastic behavior of asphalt concrete at low-temperature by fitting the model to the measured creep compliance. The model consists of multiple Voight-Kelvin elements accounting for the delayed elastic behavior assembled in series with one Maxwell element, resulting in a model that characterizes both elastic and creep responses (see Fig. 5). The creep compliance function of the generalized Voight-Kelvin model is presented in Eq. (5),

$$D(t) = D_0 + \eta t + \sum_{i=1}^N D_i(1 - \exp[-\lambda_i t]) \quad (5)$$

where D_0 and η are the spring instantaneous creep compliance and the viscosity of the dashpot, respectively, in the Maxwell element. Also, D_i are creep compliance parameters and λ_i denotes the inverse of retardation time for each Voight-Kelvin element. Considering four Kelvin elements, and minimizing the sum of squared error (SSE), the model constant coefficients including D_0 , D_i , and η were calculated as shown in Table 3. It should be mentioned that the inverse of retardation time values (λ_i) is assumed (judiciously spread across the typical time spectrum of the creep compliance master curves) and was therefore not calibrated.

4. Numerical simulation

This section presents the numerical framework for the generalized Voight-Kelvin model used to represent the viscoelastic behavior of asphalt concrete at low temperatures. It is worth mentioning

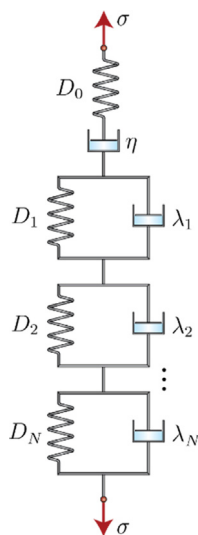


Fig. 5. The schematic of the generalized Voight-Kelvin model.

that the generalized Voight-Kelvin model is not available in the Abaqus library and needs to be implemented as a user-defined subroutine [46]. According to the schematic of the generalized Voight-Kelvin model shown in Fig. 5, the one-dimensional hereditary (Boltzmann) integration of the viscoelastic constitutive relationship results in a viscoelastic strain at time of t , which is described by:

$$\varepsilon^t = D_0 \sigma^t + \int_0^t \Delta D(\psi^t - \psi^\tau) \frac{d(\sigma^\tau)}{d\tau} d\tau + \int_0^t \eta(\psi^t - \psi^\tau) \frac{d(\sigma^\tau)}{d\tau} d\tau \quad (6)$$

where D_0 is the instantaneous compliance, ΔD is the transient creep compliance, η is the dashpot constant coefficient, τ denotes integration variable. The ε^t and σ^τ indicate strain and stress at time t , respectively. Similarly, ψ^t is the reduced time at time t , which is a function of time-temperature shift factor (a_T), as that $\psi^t = \int_0^t \frac{1}{a_T} d\xi$.

The transient compliance ΔD can be expressed using a Prony series:

$$\Delta D^{\psi^t} = \sum_{r=1}^N D_r(1 - \exp[-\lambda_r \psi^t]) \quad (7)$$

where N is the number of Prony series terms and D_r is the r th term of compliance associated with the r th retardation time, $1/\lambda_r$.

In order to solve Eq. (6) numerically, the stress, strain and internal state variables need to be determined at each time increment. Given the variables at the last time increment ($t-\Delta t$), the stress, strain, and internal state variables are calculated at the current time increment (t) and are stored for the next time increment. The numerical implicit scheme of hereditary integration for the generalized Voight-Kelvin model was implemented, as described in detail in Appendix A. As a displacement-strain-based numerical scheme, the strain tensor increment at time t (i.e., $\Delta \varepsilon_{ij}^t$) is given at the beginning of each increment. Then, given the relationship between the increment of viscoelastic strain and internal state variables stored at the last increment, the stress increment at the current time increment ($\Delta \sigma^t$) can be calculated. Finally, having the stress tensor at the last time increment ($\sigma^{t-\Delta t}$), the stress tensor at the current increment (σ^t) can be calculated as:

$$\sigma_{kl}^t = \left[D_{ijkl,0} + \sum_{r=1}^N D_{ijkl,r} - \sum_{r=1}^N D_{ijkl,r} \frac{1 - \exp[-\lambda_r \Delta \psi^t]}{\lambda_r \Delta \psi^t} + \frac{1}{2} \Delta \psi^t \eta_{ijkl} \right]^{-1} \times \left[\Delta \varepsilon_{ij}^t + \left[D_{ijkl,0} + \sum_{r=1}^N D_{ijkl,r} - \sum_{r=1}^N D_{ijkl,r} \frac{1 - \exp[-\lambda_r \Delta \psi^{t-\Delta t}]}{\lambda_r \Delta \psi^{t-\Delta t}} + \frac{1}{2} \Delta \psi^{t-\Delta t} \eta_{ijkl} \right] \sigma_{kl}^{t-\Delta t} - \left[\sum_{r=1}^N D_{ijkl,r} \frac{1 - \exp[-\lambda_r \Delta \psi^t]}{\lambda_r \Delta \psi^t} - \sum_{r=1}^N D_{ijkl,r} \frac{1 - \exp[-\lambda_r \Delta \psi^{t-\Delta t}]}{\lambda_r \Delta \psi^{t-\Delta t}} \right] \sigma_{kl}^{t-\Delta t} - \left[\frac{1}{2} \Delta \psi^{t-\Delta t} \eta_{ijkl} + \frac{1}{2} \Delta \psi^t \eta_{ijkl} \right] \sigma_{kl}^{t-\Delta t} - \left[\sum_{r=1}^N D_{ijkl,r} - \sum_{r=1}^N D_{ijkl,r} \exp[-\lambda_r \Delta \psi^t] \right] q_{kl,r}^{t-\Delta t} + \Delta \psi^t \eta_{ijkl} \sigma_{kl}^0 \right] \quad (8)$$

The expression above is given in indicial notation, and thus, the summation convention applies. Once the variables are obtained for the current time increment, the stress and strain tensors, and the internal state variables (i.e., $q_{kl,r}^t$ and p_{kl}^t), are all updated and stored for the next time increment. The numerical implementation of the

Table 3
Identified viscoelastic constant coefficient.

ID	Temp (°C)	D ₀ (1/MPa)	η (1/s/MPa)	λ ₁ (1/s)	λ ₂ (1/s)	λ ₃ (1/s)	λ ₄ (1/s)
				D ₁ (1/MPa)	D ₂ (1/MPa)	D ₃ (1/MPa)	D ₄ (1/MPa)
1824	0	6.23e-05	3.95e-07	4.14e-05	1.51e-05	2.49e-17	1.9e-04
	-12	4.52e-05	6.67e-08	1.32e-05	2.92e-06	1.04e-08	4.81e-05
	-24	3.12e-05	1.37e-08	4.53e-06	1.87e-06	5.6e-07	1.54e-05
1835	0	6.13e-05	1.76e-07	2.52e-05	1.08e-05	1.42e-08	1.07e-04
	-12	4.73e-05	4.4e-08	1.03e-05	1.4e-06	1.56e-07	3.53e-05
	-24	3.23e-05	1.71e-08	4.45e-06	2.11e-06	1.86e-06	1.49e-05
1836	0	6.53e-05	1.56e-07	2.08e-05	1.65e-05	2.2e-09	1.02e-04
	-12	4.39e-05	4.06e-08	9.22e-06	3.05e-06	4.47e-07	3.14e-05
	-24	3.02e-05	1.17e-08	2.5e-06	2.13e-06	1.3e-06	1.57e-05
1840	0	6.09e-05	2.42e-07	1.81e-05	2.19e-05	4.39e-15	1.3e-04
	-12	4.61e-05	4.61e-08	2.28e-06	1.08e-05	7.87e-06	2.12e-05
	-24	2.91e-05	1.51e-08	2.06e-06	1.74e-06	1.19e-06	1.19e-05
1844	0	5.89e-05	1.74e-07	2.86e-05	7.87e-06	5.89e-09	1.01e-04
	-12	4.13e-05	4.29e-08	1.08e-05	2.76e-06	1.29e-07	3.26e-05
	-24	2.99e-05	1.74e-08	2.9e-06	2.27e-06	1.08e-07	1.78e-05
1845	0	7.23e-05	2.72e-07	3.68e-05	1.45e-05	2.88e-11	1.46e-04
	-12	4.15e-05	5.28e-08	8.27e-06	7.27e-06	5.47e-08	3.99e-05
	-24	3.08e-05	1.27e-08	5.56e-06	1.1e-06	1.05e-08	1.8e-05

generalized Voigt-Kelvin model was implemented in the finite element code Abaqus via a user material subroutine (UMAT), following an implicit scheme.

5. Numerical validation

5.1. Comparing DC(T) response predictions with experimental measurements

In this section, the constitutive model and the introduced numerical framework are integrated to predict the time-dependent CMOD response obtained from the DC(T) test. To this end, the geometry of the DC(T) sample was modeled in Abaqus. The viscoelastic properties calculated in Section 3 were considered as constant coefficients of the model implemented in Section 4. The corresponding creep loads shown in Table 3 were applied in the model and the CMOD versus time is calculated. For instance, Fig. 6 depicts the displacement, strain, and stress fields within a DC(T) specimen at the end of a creep test.

Fig. 7 shows the CMOD response of three replicates and the corresponding FEM result for each mix compared at three different temperatures. In this figure, the range of CMOD recorded by three replicates is highlighted for each temperature. As expected, despite being subjected to the highest level of creep load, the measured CMOD response at -24 °C is always lower than the ones at -12 and 0 °C. Also, the main proportion of accumulated CMOD at -24 °C occurred at the early stages of the creep test (first ten seconds), indicating the predominant elastic behavior of the investigated asphalt mixtures at this temperature. On the other hand, the delayed elastic deformation increases as the temperature increases. As a result, the CMOD at 0 °C accumulates much more gradually in time.

The CMOD responses presented in Fig. 7 are used to validate the ability of the model to predict the DC(T) creep test results. To this end, the viscoelastic properties shown in Table 3 are implemented in the numerical framework to calculate the CMOD responses at different temperatures. Comparing the obtained CMOD responses using FEM (dashed lines in the figures) with the range of laboratory-measured CMODs in time for three replicates, shows the capability of the implemented numerical framework to successfully predict the DC(T) creep test responses. As indicated in

Section 2, the studied mixtures use various combinations of binder systems and recycled materials. However, the 1824 mix is believed to benefit from the softest binder system (SBS 64-34 binder with total ABR of 37.1% by RAP and RAS) among the SMA friction surface type mixtures. This is reflected in the CMOD response as it recorded the highest CMOD among the mixtures especially at 0 and -12 °C.

The repeatability of the DC(T) test is investigated based on the CMOD measurements at 1000 s for three replicates of each mix. Table 4 shows the standard deviation along with the measured coefficient of variance (COV) for replicate testing of the various mixture types at three temperatures. All averaged COVs are less than 10%, indicating the high level of repeatability of the DC(T) test. The highest average COV was recorded at 0 °C, which implies higher variability with higher test temperature. The higher variability of CMOD measurements at 0 °C can also be observed in Fig. 7.

5.2. Comparing IDT response predictions with experimental measurements

The viscoelastic properties of the mixtures along with the finite element method were implemented to show the capability of the numerical framework to predict the DC(T) creep responses. In this section, the viscoelastic properties obtained from DC(T) creep test are used to predict IDT creep responses. The differences in the stress state and strain distribution between the IDT and DC(T) geometries provide the opportunity to validate the DC(T) creep compliance properties and the numerical approach used in this study.

The IDT creep tests were carried out using a universal testing machine (UTM) with a capacity of 100 kN. The IDT creep test was performed on slices with 50 mm in thickness and 150 mm in diameter, following AASHTO T-322. To carry out the IDT creep test, three replicates were conditioned at 0, -12, and -24 °C. For the sample to reach the desired testing temperature, the IDT cooling chamber needed to be set at a slightly lower temperature (see Table 5). Each sample was kept at the cooling chamber for 2–4 h. The horizontal and vertical extensometers were then attached to the two faces of the IDT specimens, and the sample was placed into the IDT fixture. To compensate for the temperature loss due to

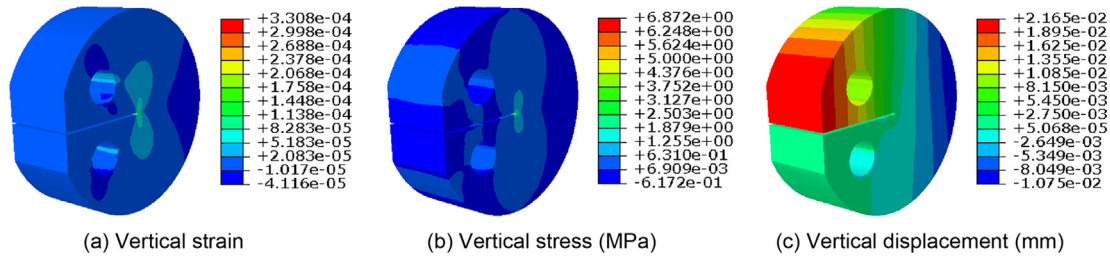


Fig. 6. An example of DC(T) creep responses as simulated with viscoelastic FEM in Abaqus.

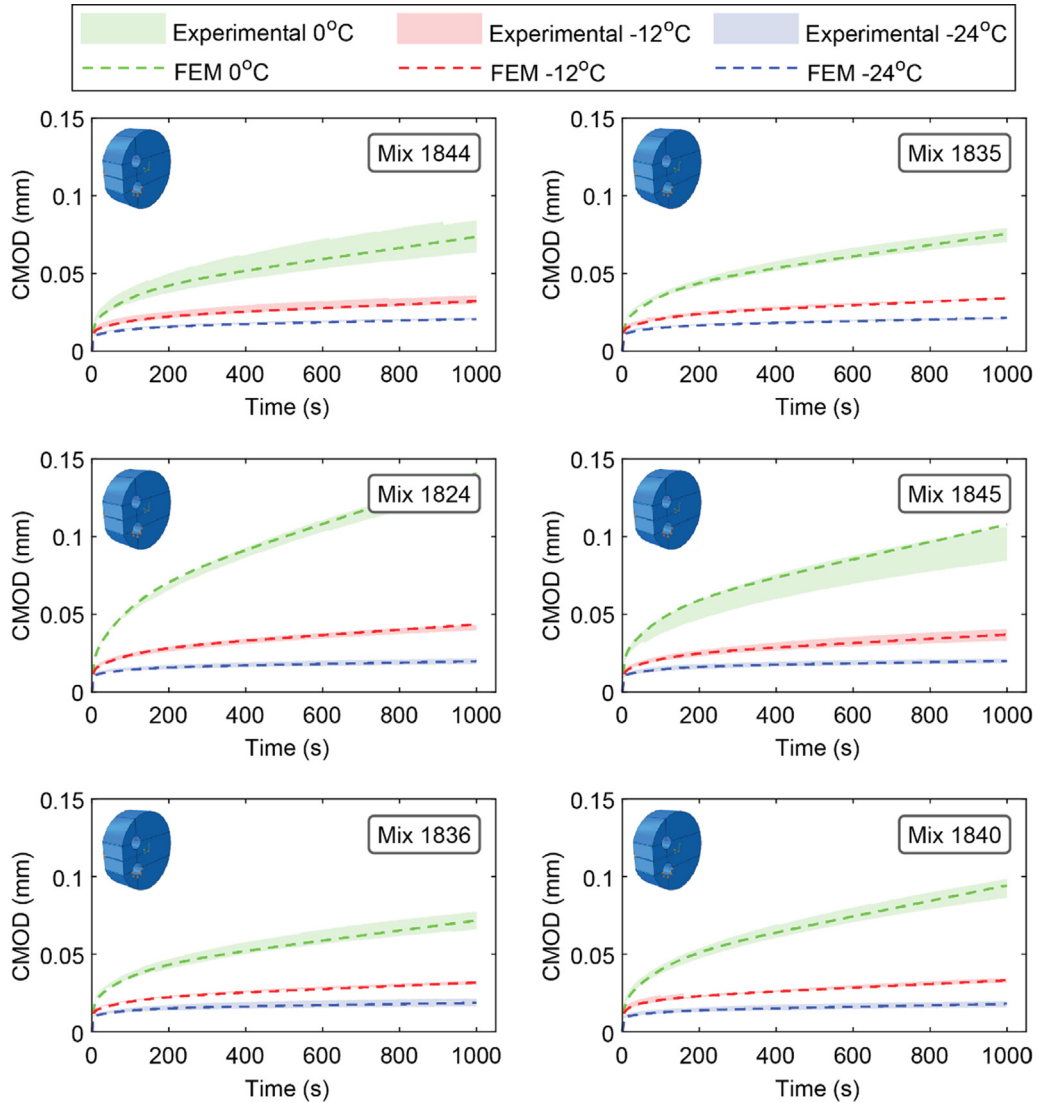


Fig. 7. CMOD response versus time at three temperature levels for mixture of: (a) 1844; (b) 1835; (c) 1824; (d) 1845; (e) 1836; (f) 1840.

opening the chamber door and installing the extensometers, the sample was kept for another half an hour to reach the testing temperature. Similar to the DC(T) creep test, a seating load of 0.1 kN was applied to the sample. The seating load fixes the sample position in the IDT fixture, ensures rapid creep loading without impact, and eliminates some of the slight nonlinearity exhibited at low load levels. In the test, the load level is rapidly increased as a steep slope-load function until the target creep load is reached. The closed-loop controls are tuned such that the creep load is attained

in less than one second. As Table 5 shows, the creep load was then maintained for 1000 s while horizontal and vertical displacements were recorded.

Fig. 8 shows the 3-D model of the IDT geometry along with the mechanical responses such as vertical stress and strain in Abaqus software. The viscoelastic properties identified from DC(T) creep test, as in Section 3, were used in numerical simulations. These mechanical responses are calculated using the viscoelastic parameters presented in Table 3 obtained from the DC(T) creep test. It is

Table 4
Repeatability of CMOD at 1000 s.

Mix. ID	−24 °C		−12 °C		0 °C	
	STD (mm)	COV (%)	STD (mm)	COV (%)	STD (mm)	COV (%)
1844	0.0004	2.0	0.0029	8.8	0.0102	14.0
1835	0.0002	1.1	0.0005	1.5	0.0044	6.0
1824	0.0016	8.3	0.0028	6.7	0.0050	3.7
1845	0.0015	7.3	0.0035	9.5	0.0107	11.0
1836	0.0022	11.8	0.0013	4.2	0.0062	8.8
1840	0.0017	9.2	0.0012	3.7	0.0102	14.0
AVG	0.0013	6.6	0.0020	5.7	0.0078	9.6

worth mentioning that the IDT test possesses a multiaxial stress state such that the vertical and horizontal stresses are imposed in vertical and horizontal directions, respectively. Given that the stress state in the DC(T) test is different than that in the IDT test (both in magnitude and distribution), a comparison between the results from both tests provides a meaningful way to verify and validate the ability of the proposed approach to identify the viscoelastic properties of asphalt mixtures at low temperatures.

To conduct the IDT test per AASHTO T-322, three replicates were tested for each mixture at three temperatures. As the extensometers are mounted on both sides of the IDT sample, six horizontal and six vertical sets of deflections were collected. Then, the maximum and minimum measure deflection were discarded (trimmed) per AASHTO T-322 and four extensometer results were used to analyze the results. Figs. 9–14 show the response range of the four extensometer measurements at each direction and the corresponding FEM result for mixtures at three different temperatures under the IDT test. The horizontal and vertical displacements measured in each test were compared against the corresponding numerical results. The close agreement between the numerical simulations and experimental measurements validates the viscoelastic properties acquired through the proposed approach and the DC(T) creep test results.

Tables 6 and 7 provide the IDT test repeatability measures in the horizontal and vertical directions, respectively, using the extensometer measurements at 1000 s. The STD and COV parameters are calculated after discarding the lowest and highest measured deflections and considering the results from the remaining four extensometers in each direction, following AASHTO T-322. Using the trimmed data set from the three tested replicates leads to a lower coefficient of variation. According to Tables 6 and 7, the averaged COV of the mixtures ranges from 9.0 to 16% in horizontal and 9.8 to 12.7% in vertical directions. Comparing to the DC(T) creep test repeatability, the COV of the IDT creep test is slightly higher. Also, it could be observed in both DC(T) and IDT tests that warmer test temperature leads to a higher standard deviation. As a result, a higher discrepancy is observed between the measured deflections and FEM predictions at 0 and −12 °C as compared to −24 °C (Figs. 9–14).

Table 8 presents a variety of items that could be considered to further compare the IDT and DC(T) creep tests. The DC(T) sample fabrication involves additional steps such as making the notch and coring the holes. Therefore, the IDT sample fabrication is easier than that of the DC(T) sample. Although the vertical and horizontal

extensometers on the sample surface make the instrumentation of the IDT test more difficult than that of the DC(T), it provides the chance to determine the Poisson’s ratio of the mixture. Due to the measurement of the deflection in only one dimension in the DC(T) test, the calculation of Poisson’s ratio is not possible through the presented DC(T) test setup. Monitoring the temperature of the asphalt sample in the cooling chamber indicated that a shorter duration of conditioning times is needed for temperature equilibrium in the DC(T) test. Also, opening the chamber door to load the testing into the test fixture has a small negative effect on the temperature of the conditioned sample. These resulted in selecting the DC(T) creep test as the more efficient test in terms of the temperature controlling system. Given the lower COV calculated for these two tests, despite the trimmed data procedure applied for IDT displacing measurements, it was concluded that the DC(T) test is more repeatable than the IDT creep test. The DC(T) creep test is also preferable in terms of the equipment cost and ease of data analysis.

6. Summary, conclusions, and future work

In this study, a new method called the DC(T) creep test was introduced to characterize the viscoelastic behavior of asphalt mixtures at low temperatures. To this end, the CMOD responses of six SMA type mixtures were measured under a constant load applied to the sample in 1000 s at three temperatures including −24, −12, and 0 °C. According to the well-known correspondence principle in viscoelastic studies, the CMOD measurements under the DC(T) test along with a correction factor that accounts for the sample geometry were used to calculate the creep compliance as a function of time. A generalized Voight-Kelvin model including an isolated spring, a dashpot, and four Kelvin elements was employed and calibrated for each mix at each of the test temperatures. The viscoelastic constitutive relationship was implemented in the finite element code Abaqus via a user material subroutine. The proposed numerical framework was used to predict the DC(T) response under creep loading. In addition, IDT creep tests were conducted at the same temperatures and the horizontal and vertical displacements were measured. The developed framework and determined viscoelastic parameters from the DC(T) creep tests were implemented to predict the IDT responses. The following conclusions could be drawn from the test results and analysis presented:

Table 5
Loading properties in IDT creep test.

Test	Testing Temp. (°C)	Chamber Temp. (°C)	Seating Load (kN)	Ramp Time (s)	Creep Load (kN)	Creep Time (s)
IDT creep	0	−1.5	0.1	1	4	1000
	−12	−14		1	8	
	−24	−26		1	20	

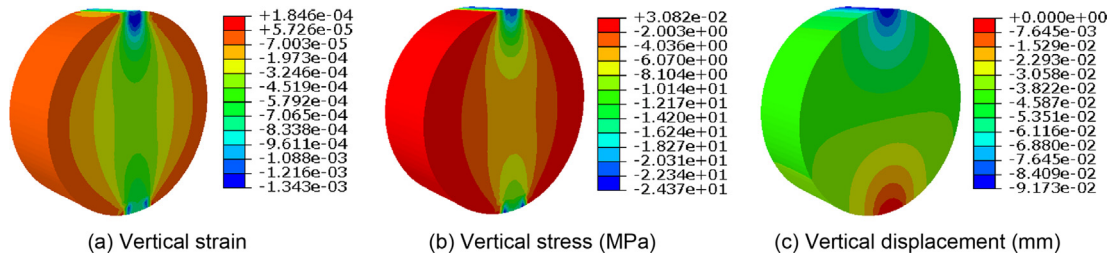


Fig. 8. An example of IDT creep responses through FEM.

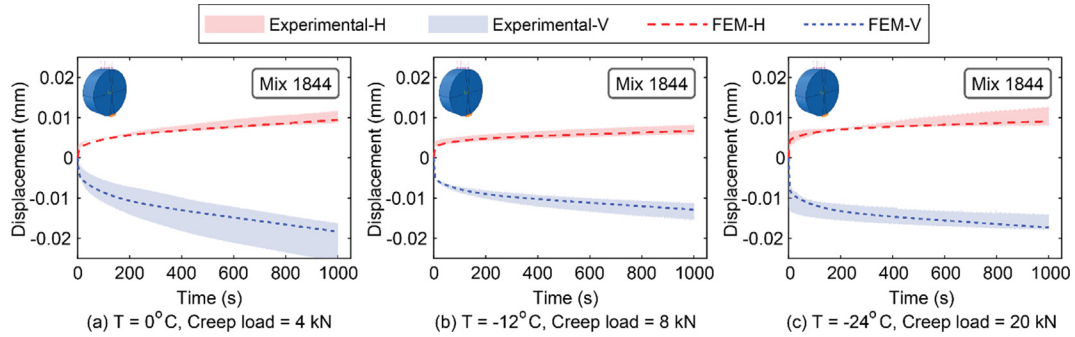


Fig. 9. Horizontal and vertical deflections from IDT testing for the 1844 mix: (a) at 0 °C; (b) at -12 °C; (c) at -24 °C.

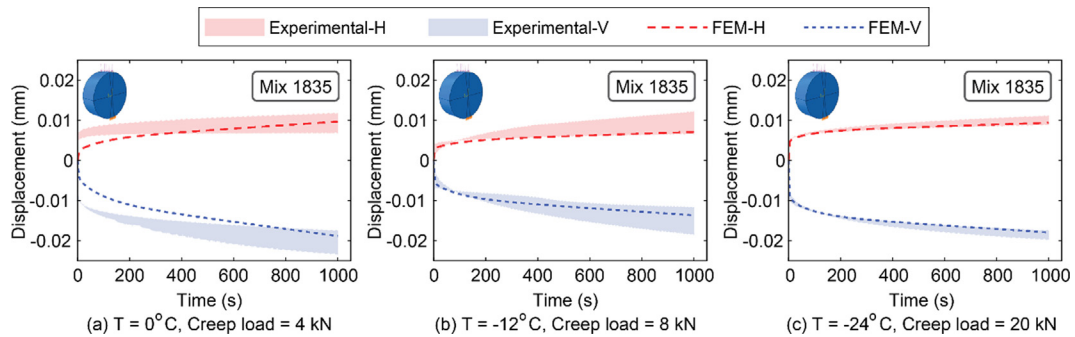


Fig. 10. Horizontal and vertical deflections from IDT testing for the 1835 mix: (a) at 0 °C; (b) at -12 °C; (c) at -24 °C.

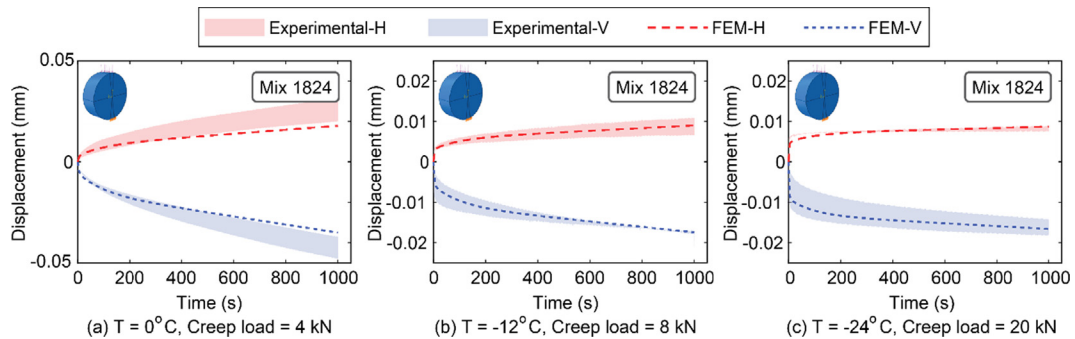


Fig. 11. Horizontal and vertical deflections from IDT testing for the 1824 mix: (a) at 0 °C; (b) at -12 °C; (c) at -24 °C.

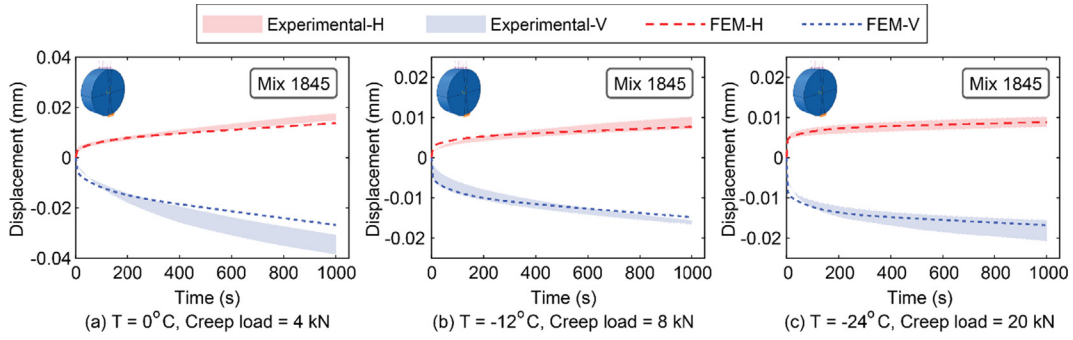


Fig. 12. Horizontal and vertical deflections from IDT testing for the 1845 mix: (a) at 0 °C; (b) at -12 °C; (c) at -24 °C.

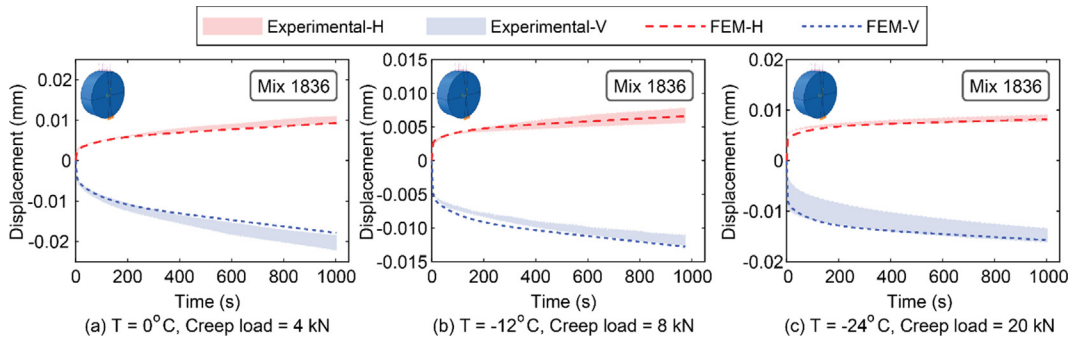


Fig. 13. Horizontal and vertical deflections from IDT testing for the 1836 mix: (a) at 0 °C; (b) at -12 °C; (c) at -24 °C.

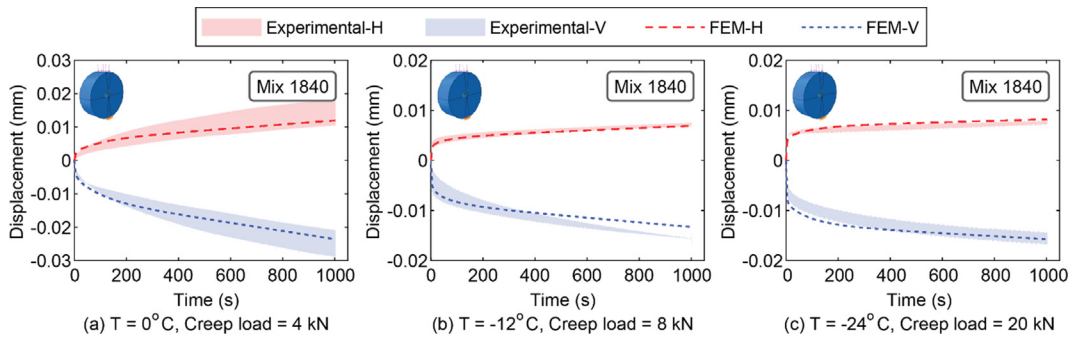


Fig. 14. Horizontal and vertical deflections from IDT testing for the 1840 mix: (a) at 0 °C; (b) at -12 °C; (c) at -24 °C.

Table 6
 Repeatability of IDT creep horizontal displacement at 1000 s.

Mix. ID	-24 °C		-12 °C		0 °C	
	STD (mm)	COV (%)	STD (mm)	COV (%)	STD (mm)	COV (%)
1844	0.0020	18.8	0.0009	13.2	0.0014	13.1
1835	0.0010	10.6	0.0027	31.8	0.0020	21.6
1824	0.0007	8.0	0.0017	19.8	0.0050	18.4
1845	0.0011	12.3	0.0013	15.4	0.0011	7.0
1836	0.0005	6.1	0.0012	17.5	0.0008	7.8
1840	0.0003	3.6	0.0005	7.5	0.0038	28.1
AVG	0.0009	9.9	0.0014	17.5	0.0023	16.0

Table 7
Repeatability of IDT creep vertical displacement at 1000 s.

Mix. ID	-24 °C		-12 °C		0 °C	
	STD (mm)	COV (%)	STD (mm)	COV (%)	STD (mm)	COV (%)
1844	0.0017	11.0	0.0017	12.5	0.0041	19.7
1835	0.0012	6.0	0.0033	24.5	0.0024	11.9
1824	0.0018	11.1	0.0035	18.4	0.0054	12.9
1845	0.0024	12.9	0.0006	3.7	0.0033	9.2
1836	0.0013	8.8	0.0008	7.0	0.0017	8.1
1840	0.0014	8.8	0.0012	8.2	0.0035	14.5
AVG	0.0016	9.8	0.0019	12.4	0.0034	12.7

Table 8
Comparing IDT with DC(T) creep tests.

	DC(T) creep	IDT creep
Easier sample fabrication		✓
Also measures Poisson's ratio		✓
Easier instrumentation	✓	
Better temperature control	✓	
Higher test repeatability	✓	
Less expensive equipment	✓	
Simpler analysis	✓	

- The relationship between the CMOD response measured in the DC(T) creep test and the resulting viscoelastic creep compliance obtained by applying the simple geometrical constant developed herein can be used to simply and accurately characterize the viscoelastic creep behavior of asphalt concrete at low temperatures.
- The developed numerical framework and UMAT subroutine for the generalized Voight-Kelvin model can be used to simulate the viscoelastic response of asphalt mixtures in the commercial FEM code ABAQUS.
- The close agreement between the laboratory-measured displacements in the IDT test and the FEM predicted displacements validated the viscoelastic properties obtained with the newly proposed DC(T) creep test and analysis method.
- The DC(T) creep test yields a lower COVs and is deemed to be more repeatable than the IDT creep test, even after applying the trimmed mean approach to the displacements measured in the IDT test.
- Except for the easier sample fabrication and the possibility to calculate Poisson's ratio, the DC(T) creep test may be viewed as preferable over the IDT creep test in terms of the added simplicity and reduced cost for instrumentation, temperature control, and data analysis.

More work will be needed to further develop and apply the DC (T) creep test method presented in this study. These research needs include the following: 1) a more accurate and systemic estimation of the creep loading level that is high enough to avoid problems associated with noise and low enough to prevent nonlinearity; 2) investigating a variety of asphalt mixtures including densegraded with different aggregate structure, binder type, and modification; 3) implementing the DC(T) creep results in software tools such as Pavement-ME and Illi-TC to predict the low temperature cracking performance of asphalt pavements during the service life.

CRedit authorship contribution statement

Behnam Jahangiri: Investigation, Formal analysis, Writing - original draft. **Mohammad M. Karimi:** Formal analysis, Software, Writing - original draft. **Oliver Giraldo-Londoño:** Software, Writ-

ing - review & editing, Visualization. **William G. Buttlar:** Supervision, Conceptualization, Writing - review & editing.

Declaration of Competing Interest

The authors declare that they have no known competing financial interests or personal relationships that could have appeared to influence the work reported in this paper.

Acknowledgments

The authors would like to thank the Illinois State Toll Highway Authority for their assistance and generous support of this research during the various stages of this research investigation. Finally, this research team would like to thank James Meister, and Grant Nichols from Mizzou Asphalt Pavement and Innovation Laboratory (MAPIL) for their assistance in during the course of this study.

Appendix A. Numerical derivation for the generalized Kelvin-Voight model

According to the schematic of the generalized Voigt-Kelvin model shown in Fig. 5, the one-dimensional hereditary (Boltzmann) integration of viscoelastic constitutive relationship results in the viscoelastic strain at the time of t , such that:

$$\varepsilon^t = D_0\sigma^t + \int_0^t \Delta D^{(\psi^t - \psi^\tau)} \frac{d(\sigma^\tau)}{d\tau} d\tau + \int_0^t \eta(\psi^t - \psi^\tau) \frac{d(\sigma^\tau)}{d\tau} d\tau \quad (A1)$$

where D_0 is the instantaneous compliance, ΔD is the transient creep compliance, η is the dashpot constant coefficient, τ denotes integration variable. The ε^t and σ^τ indicate strain and stress at time t , respectively. Similarly, ψ^t is the reduced time at time t , which is a function of time-temperature shift factor(a_T), as that $\psi^t = \int_0^t \frac{1}{a_T} d\xi$. The transient compliance ΔD can be expressed using a Prony series:

$$\Delta D^{\psi^t} = \sum_{r=1}^N D_r (1 - \exp[-\lambda_r \psi^t]) \quad (A2)$$

where N is the number of Prony series terms and D_r is the r th term of compliance associated with the r th retardation time, $1/\lambda_r$. The general three-dimensional form of hereditary integration mentioned in Eq. (A1) can be re-written as

$$\varepsilon_{ij}^t = D_{ijkl,0} \sigma_{kl}^t + \int_0^t \Delta D_{ijkl}^{(\psi^t - \psi^\tau)} \frac{d(\sigma_{kl}^\tau)}{d\tau} d\tau + \int_0^t \eta_{ijkl}(\psi^t - \psi^\tau) \times \frac{d(\sigma_{kl}^\tau)}{d\tau} d\tau \quad (A3)$$

where

$$\Delta D_{ijkl}^{\psi^t} = \sum_{r=1}^N D_{ijkl,r} (1 - \exp[-\lambda_r \psi^t]) \quad (A4)$$

Substituting Eq. (A4) into Eq. (A3), the viscoelastic strain at time t can be written as:

$$\epsilon_{ij}^t = D_{ijkl,0} \sigma_{kl}^t + \sum_{r=1}^N D_{ijkl,r} \sigma_{kl}^t - \sum_{r=1}^N D_{ijkl,r} q_{kl,r}^t + \eta_{ijkl} p_{kl}^t \quad (A5)$$

where

$$q_{kl,r}^t = \int_0^t \exp[-\lambda_r(\psi^t - \psi^\tau)] \frac{d(\sigma_{kl}^\tau)}{d\tau} d\tau \quad (A6)$$

$$p_{kl}^t = \int_0^t (\psi^t - \psi^\tau) \frac{d(\sigma_{kl}^\tau)}{d\tau} d\tau$$

The terms $q_{kl,r}^t$ and p_{kl}^t denote the history part of the hereditary (Boltzmann) integration. To develop a recursive and numerical scheme, $q_{kl,r}^t$ is decomposed into two terms, as follows:

$$q_{kl,r}^t = \int_0^{t-\Delta t} \exp[-\lambda_r(\psi^t - \psi^\tau)] \frac{d(\sigma_{kl}^\tau)}{d\tau} d\tau + \int_{t-\Delta t}^t \exp[-\lambda_r(\psi^t - \psi^\tau)] \frac{d(\sigma_{kl}^\tau)}{d\tau} d\tau \quad (A7)$$

The first part of the integral in Eq. (A7) can be simplified as:

$$\begin{aligned} \int_0^{t-\Delta t} \exp[-\lambda_r(\psi^t - \psi^\tau)] \frac{d(\sigma_{kl}^\tau)}{d\tau} d\tau &= (\exp[-\lambda_r(\Delta\psi^t)]) \\ &= \int_0^{t-\Delta t} \exp[-\lambda_r(\psi^{t-\Delta t} - \psi^\tau)] \frac{d(\sigma_{kl}^\tau)}{d\tau} d\tau \\ &= \exp[-\lambda_r(\Delta\psi^t)] q_{kl,r}^{t-\Delta t}; \quad \Delta\psi^t = \psi^t - \psi^{t-\Delta t} \end{aligned} \quad (A8)$$

The term $q_{kl,r}^{t-\Delta t}$ is the hereditary integral for every term of the Prony series and should be updated and stored at the end of the previous increment $t - \Delta t$. This history term will be used to update the stress tensor at the current time, t . For small time increments, Δt , the term σ_{kl}^τ can be assumed to be linear over $t - \Delta t \leq \tau \leq t$ (i.e., $\frac{d(\sigma_{kl}^\tau)}{d\tau} \approx \frac{\sigma_{kl}^t - \sigma_{kl}^{t-\Delta t}}{\Delta\psi^t}$). Therefore, the second term of the integration in Eq. (A7) is simplified as:

$$\begin{aligned} \int_{t-\Delta t}^t \exp[-\lambda_r(\psi^t - \psi^\tau)] \frac{d(\sigma_{kl}^\tau)}{d\tau} d\tau \\ = [\sigma_{kl}^t - \sigma_{kl}^{t-\Delta t}] \frac{1 - \exp[-\lambda_r \Delta\psi^t]}{\lambda_r \Delta\psi^t} \end{aligned} \quad (A9)$$

Therefore, by substituting Eqs. (A8) and (A9) into Eq. (A7), the term $q_{kl,r}^t$ simplifies to

$$q_{kl,r}^t = \exp[-\lambda_r(\Delta\psi^t)] q_{kl,r}^{t-\Delta t} + [\sigma_{kl}^t - \sigma_{kl}^{t-\Delta t}] \frac{1 - \exp[-\lambda_r \Delta\psi^t]}{\lambda_r \Delta\psi^t} \quad (A10)$$

Similarly, the second part of Eq. (A6) is re-written as:

$$\begin{aligned} p_{kl}^t &= \int_0^t (\psi^t - \psi^\tau) \frac{d(\sigma_{kl}^\tau)}{d\tau} d\tau \\ &= \int_0^{t-\Delta t} (\psi^t - \psi^\tau) \frac{d(\sigma_{kl}^\tau)}{d\tau} d\tau + \int_{t-\Delta t}^t (\psi^t - \psi^\tau) \frac{d(\sigma_{kl}^\tau)}{d\tau} d\tau \end{aligned} \quad (A11)$$

where

$$\begin{aligned} p_{kl}^t &= \int_0^{t-\Delta t} (\psi^t - \Delta\psi^t + \Delta\psi^t - \psi^\tau) \frac{d(\sigma_{kl}^\tau)}{d\tau} d\tau + \int_{t-\Delta t}^t (\psi^t - \psi^\tau) \frac{d(\sigma_{kl}^\tau)}{d\tau} d\tau \\ &= \int_0^{t-\Delta t} (\psi^t - \Delta\psi^t - \psi^\tau) \frac{d(\sigma_{kl}^\tau)}{d\tau} d\tau + t - \Delta t \int_0^{t-\Delta t} \Delta\psi^t \frac{d(\sigma_{kl}^\tau)}{d\tau} d\tau + \int_{t-\Delta t}^t (\psi^t - \psi^\tau) \frac{d(\sigma_{kl}^\tau)}{d\tau} d\tau \end{aligned} \quad (A12)$$

For small time increments, Δt , the term σ_{kl}^τ can be assumed to be linear over $t - \Delta t \leq \tau \leq t$. Therefore, Eq. (A12) reduces to:

$$\begin{aligned} p_{kl}^t &= p_{kl}^{t-\Delta t} + \int_0^{t-\Delta t} \Delta\psi^t \frac{d(\sigma_{kl}^\tau)}{d\tau} d\tau + \int_{t-\Delta t}^t (\psi^t - \psi^\tau) \frac{d(\sigma_{kl}^\tau)}{d\tau} d\tau \\ &= p_{kl}^{t-\Delta t} + \Delta\psi^t [\sigma_{kl}^t - \sigma_{kl}^{t-\Delta t}] + [\psi^t - \psi^{t-\Delta t}] \frac{d(\sigma_{kl}^\tau)}{d\tau} \Big|_{t-\Delta t}^t \\ &= p_{kl}^{t-\Delta t} + \Delta\psi^t [\sigma_{kl}^{t-\Delta t} - \sigma_{kl}^0] + \frac{1}{2} \Delta\psi^t [\sigma_{kl}^t - \sigma_{kl}^{t-\Delta t}] \end{aligned} \quad (A13)$$

Substituting Eqs. (A10) and (A13) into Eq. (A5), the viscoelastic strain at time t can be expressed as follows:

$$\epsilon_{ij}^t = \bar{D}_{ijkl}^t \sigma_{kl}^t - H_{ij}^t \quad (A14)$$

where

$$\begin{aligned} \bar{D}_{ijkl}^t &= D_{ijkl,0} + \sum_{r=1}^N D_{ijkl,r} - \sum_{r=1}^N D_{ijkl,r} \frac{1 - \exp[-\lambda_r \Delta\psi^t]}{\lambda_r \Delta\psi^t} \\ &\quad + \frac{1}{2} \Delta\psi^t \eta_{ijkl} \end{aligned} \quad (A15)$$

and

$$\begin{aligned} H_{ij}^t &= \sum_{r=1}^N D_{ijkl,r} q_{kl,r}^{t-\Delta t} \exp[-\lambda_r \Delta\psi^t] - \sum_{r=1}^N D_{ijkl,r} \sigma_{kl}^{t-\Delta t} \frac{1 - \exp[-\lambda_r \Delta\psi^t]}{\lambda_r \Delta\psi^t} \\ &\quad - \eta_{ijkl} p_{kl}^{t-\Delta t} - \Delta\psi^t [\eta_{ijkl} \sigma_{kl}^{t-\Delta t} - \eta_{ijkl} \sigma_{kl}^0] + \frac{1}{2} \Delta\psi^t \eta_{ijkl} \sigma_{kl}^{t-\Delta t} \end{aligned} \quad (A16)$$

The term H_{ij}^t in Eq. (A16) is a function of $q_{kl,r}^{t-\Delta t}$ and $p_{kl}^{t-\Delta t}$, which depend on the history of loading at the time $t - \Delta t$. In order to make the H_{ij}^t as a function of the internal state variables at time t , according to Eqs. (A10) and (A13), term $\exp[-\lambda_r(\Delta\psi^t)] q_{kl,r}^{t-\Delta t}$ and $p_{kl}^{t-\Delta t}$ can be written as:

$$\begin{aligned} \exp[-\lambda_r(\Delta\psi^t)] q_{kl,r}^{t-\Delta t} &= q_{kl,r}^t - [\sigma_{kl}^t - \sigma_{kl}^{t-\Delta t}] \frac{1 - \exp[-\lambda_r \Delta\psi^t]}{\lambda_r \Delta\psi^t} \\ p_{kl}^{t-\Delta t} &= p_{kl}^t - \Delta\psi^t [\sigma_{kl}^{t-\Delta t} - \sigma_{kl}^0] - \frac{1}{2} \Delta\psi^t [\sigma_{kl}^t - \sigma_{kl}^{t-\Delta t}] \end{aligned} \quad (A17)$$

Therefore, Eq. (A16) is simplified and presented as a function of variables at the time t , such that:

$$\begin{aligned} H_{ij}^t &= \sum_{r=1}^N D_{ijkl,r} q_{kl,r}^t - \sigma_{kl}^t \sum_{r=1}^N D_{ijkl,r} \frac{1 - \exp[-\lambda_r \Delta\psi^t]}{\lambda_r \Delta\psi^t} \\ &\quad - \eta_{ijkl} p_{kl}^t + \frac{1}{2} \eta_{ijkl} \Delta\psi^t \sigma_{kl}^t \end{aligned} \quad (A18)$$

The current increment of viscoelastic strain can be obtained as:

$$\begin{aligned} \Delta\epsilon_{ij}^t &= \epsilon_{ij}^t - \epsilon_{ij}^{t-\Delta t}; \\ \epsilon_{ij}^t &= \bar{D}_{ijkl}^t \sigma_{kl}^t - H_{ij}^t; \\ \epsilon_{ij}^{t-\Delta t} &= \bar{D}_{ijkl}^{t-\Delta t} \sigma_{kl}^{t-\Delta t} - H_{ij}^{t-\Delta t} \end{aligned} \quad (A19)$$

Therefore, the strain increment at the time of t is written such that:

$$\Delta\epsilon_{ij}^t = \bar{D}_{ijkl}^t \sigma_{kl}^t - \bar{D}_{ijkl}^{t-\Delta t} \sigma_{kl}^{t-\Delta t} - (H_{ij}^t - H_{ij}^{t-\Delta t}) \quad (A20)$$

where

$$\begin{aligned} \bar{D}_{ijkl}^{t-\Delta t} &= D_{ijkl,0} + \sum_{r=1}^N D_{ijkl,r} - \sum_{r=1}^N D_{ijkl,r} \frac{1 - \exp[-\lambda_r \Delta\psi^{t-\Delta t}]}{\lambda_r \Delta\psi^{t-\Delta t}} + \frac{1}{2} \Delta\psi^{t-\Delta t} \eta_{ijkl} \\ H_{ij}^{t-\Delta t} &= \sum_{r=1}^N D_{ijkl,r} q_{kl,r}^{t-\Delta t} - \sigma_{kl}^{t-\Delta t} \sum_{r=1}^N D_{ijkl,r} \frac{1 - \exp[-\lambda_r \Delta\psi^{t-\Delta t}]}{\lambda_r \Delta\psi^{t-\Delta t}} \\ &\quad - \eta_{ijkl} p_{kl}^{t-\Delta t} + \frac{1}{2} \eta_{ijkl} \Delta\psi^{t-\Delta t} \sigma_{kl}^{t-\Delta t} \end{aligned} \quad (A21)$$

According to Eqs. (A19) to (A21), the increment of viscoelastic strain at time t can be expressed as a function of the stress at current time t and the stress and loading history at the previous increment, $t - \Delta t$, as follows:

$$\begin{aligned} \Delta \epsilon_{ij}^t &= D_{ijkl}^t \sigma_{kl}^t - D_{ijkl}^{t-\Delta t} \sigma_{kl}^{t-\Delta t} - (H_{ij}^t - H_{ij}^{t-\Delta t}) = \\ &\left[D_{ijkl,0} + \sum_{r=1}^N D_{ijkl,r} - \sum_{r=1}^N D_{ijkl,r} \frac{1 - \exp[-\lambda_r \Delta \psi^t]}{\lambda_r \Delta \psi^t} + \frac{1}{2} \Delta \psi^t \eta_{ijkl} \right] \sigma_{kl}^t \\ &- \left[D_{ijkl,0} + \sum_{r=1}^N D_{ijkl,r} - \sum_{r=1}^N D_{ijkl,r} \frac{1 - \exp[-\lambda_r \Delta \psi^{t-\Delta t}]}{\lambda_r \Delta \psi^{t-\Delta t}} + \frac{1}{2} \Delta \psi^{t-\Delta t} \eta_{ijkl} \right] \sigma_{kl}^{t-\Delta t} \\ &+ \left[\sum_{r=1}^N D_{ijkl,r} \frac{1 - \exp[-\lambda_r \Delta \psi^t]}{\lambda_r \Delta \psi^t} - \sum_{r=1}^N D_{ijkl,r} \frac{1 - \exp[-\lambda_r \Delta \psi^{t-\Delta t}]}{\lambda_r \Delta \psi^{t-\Delta t}} \right] \sigma_{kl}^{t-\Delta t} \\ &+ \left[\frac{1}{2} \Delta \psi^{t-\Delta t} \eta_{ijkl} + \frac{1}{2} \Delta \psi^t \eta_{ijkl} \right] \sigma_{kl}^{t-\Delta t} \\ &+ \left[\sum_{r=1}^N D_{ijkl,r} - \sum_{r=1}^N D_{ijkl,r} \exp[-\lambda_r \Delta \psi^t] \right] q_{kl,r}^{t-\Delta t} \\ &- \Delta \psi^t \eta_{ijkl} \sigma_{kl}^0 \end{aligned} \tag{A22}$$

As a displacement-strain-based numerical scheme, the strain tensor increment at time t (i.e., $\Delta \epsilon_{ij}^t$) is given at the beginning of each increment. Solving Eq. (A22) considering the strain tensor increment and loading history at the previous increment, the stress tensor at the current increment can be calculated as:

$$\begin{aligned} \sigma_{kl}^t &= \left[D_{ijkl,0} + \sum_{r=1}^N D_{ijkl,r} - \sum_{r=1}^N D_{ijkl,r} \frac{1 - \exp[-\lambda_r \Delta \psi^t]}{\lambda_r \Delta \psi^t} + \frac{1}{2} \Delta \psi^t \eta_{ijkl} \right]^{-1} \times \\ &\left[\Delta \epsilon_{ij}^t + \left[D_{ijkl,0} + \sum_{r=1}^N D_{ijkl,r} - \sum_{r=1}^N D_{ijkl,r} \frac{1 - \exp[-\lambda_r \Delta \psi^{t-\Delta t}]}{\lambda_r \Delta \psi^{t-\Delta t}} + \frac{1}{2} \Delta \psi^{t-\Delta t} \eta_{ijkl} \right] \sigma_{kl}^{t-\Delta t} \right. \\ &\left. - \left[\sum_{r=1}^N D_{ijkl,r} \frac{1 - \exp[-\lambda_r \Delta \psi^t]}{\lambda_r \Delta \psi^t} - \sum_{r=1}^N D_{ijkl,r} \frac{1 - \exp[-\lambda_r \Delta \psi^{t-\Delta t}]}{\lambda_r \Delta \psi^{t-\Delta t}} \right] \sigma_{kl}^{t-\Delta t} \right. \\ &\left. - \left[\frac{1}{2} \Delta \psi^{t-\Delta t} \eta_{ijkl} + \frac{1}{2} \Delta \psi^t \eta_{ijkl} \right] \sigma_{kl}^{t-\Delta t} - \left[\sum_{r=1}^N D_{ijkl,r} - \sum_{r=1}^N D_{ijkl,r} \exp[-\lambda_r \Delta \psi^t] \right] q_{kl,r}^{t-\Delta t} \right. \\ &\left. + \Delta \psi^t \eta_{ijkl} \sigma_{kl}^0 \right] \end{aligned} \tag{A23}$$

The stress and strain tensors and internal state variables (i.e., $q_{kl,r}^t$ and p_{kl}^t) are updated and stored for the next time increment.

References

- [1] H. Jahanbakhsh, M. M. Karimi, F. Moghadas Nejad, B. Jahangiri, Viscoelastic-based approach to evaluate low temperature performance of asphalt binders, *Constr. Build. Mater.* 128 (2016) 384–398, <https://doi.org/10.1016/j.conbuildmat.2016.10.073>.
- [2] R. Roque, W.G. Buttlar, The development of a measurement and analysis system to accurately determine asphalt concrete properties using the indirect tensile mode (with discussion), *J. Assoc. Asph. Paving Technol.* 61 (1992).
- [3] J.P. Hallin, Development of the 2002 guide for the design of new and rehabilitated pavement structures: Phase II, Rep. Natl. Coop. Highw. Res. Program, Transp. Res. Board, Natl. Res. Council. (2004).
- [4] M.O. Marasteanu, X. Li, T.R. Clyne, V.R. Voller, D.H. Timm, D.E. Newcomb, Low Temperature Cracking of Asphalt Concrete Pavements, (2004) 210.
- [5] E.V. Dave, W.G. Buttlar, S.E. Leon, B. Behnia, G.H. Paulino, IlliTC - low-temperature cracking model for asphalt pavements, *Road Mater. Pavement Des.* 14 (sup2) (2013) 57–78, <https://doi.org/10.1080/14680629.2013.812838>.
- [6] B. Jahangiri, P. Rath, H. Majidifard, L. Urra, W.G. Buttlar, Investigation of recycled asphalt mixtures in Missouri: laboratory, field, and ILLI-TC modelling, *Road Mater. Pavement Des.* (2021), <https://doi.org/10.1080/14680629.2021.1888778>.
- [7] B. Jahangiri, M.M. Karimi, N. Tabatabaee, Relaxation of hardening in asphalt concrete under cyclic compression loading, *J. Mater. Civ. Eng.* 29 (5) (2017) 04016288, [https://doi.org/10.1061/\(ASCE\)JMT.1943-5533.0001814](https://doi.org/10.1061/(ASCE)JMT.1943-5533.0001814).
- [8] M.E. Tuttle, H.F. Brinson, Prediction of the long-term creep compliance of general composite laminates, *Exp. Mech.* 26 (1) (1986) 89–102, <https://doi.org/10.1007/BF02319961>.
- [9] E. Zegeye Teshale, H.K. Stolarski, M.O. Marasteanu, Determination of Creep Compliance of Asphalt Concrete from Notched Semi-Circular Bend (SCB) Test, *Exp. Mech.* 53 (6) (2013) 919–928, <https://doi.org/10.1007/s11340-012-9688-z>.
- [10] C.E.N. EN, 12697-46: Bituminous Mixtures—Test Methods for Hot Mix Asphalt—Part: 46: Low Temperature Cracking and Properties by Uniaxial Tension Tests, Eur. Comm. Stand. CEN Paris, Fr. (2012).
- [11] M.J. Farrar, E.Y. Hajj, J.-P. Planche, M.Z. Alavi, A method to estimate the thermal stress build-up in an asphalt mixture from a single-cooling event, *Road Mater. Pavement Des.* 14 (sup1) (2013) 201–211, <https://doi.org/10.1080/14680629.2013.774756>.
- [12] A. T322, Standard Method of Test Detemining the Creep Compliance and Strength of Hot Mix Asphalt (HMA) Using the Indirect Tensile Test Device, Am. Assoc. State Highw. Transp. Off. 07 (2007).
- [13] W.G. Buttlar, R. Roque, Development and evaluation of the strategic highway research program measurement and analysis system for indirect tensile testing at low temperatures, *Transp. Res. Rec.* (1994).
- [14] Adam Zofka, Mihai Marasteanu, Mugurel Turos, Investigation of asphalt mixture creep compliance at low temperatures, *Road Mater. Pavement Des.* 9 (sup1) (2008) 269–285, <https://doi.org/10.1080/14680629.2008.9690169>.
- [15] AASHTO T313-05, Standard Method of Test for Determining the Flexural Creep Stiffness of Asphalt Binder Using the Bending Beam Rheometer (BBR), Stand. Specif. Transp. Mater. Methods Sampl. Test. 12 (2005) 1–23, <https://doi.org/10.1520/D6648-08R16.2>.
- [16] Józef Judycki, Verification of the new viscoelastic method of thermal stress calculation in asphalt layers of pavements, *Int. J. Pavement Eng.* 19 (8) (2018) 725–737, <https://doi.org/10.1080/10298436.2016.1199883>.
- [17] Raul A. Velásquez, Joseph F. Labuz, Mihai O. Marasteanu, Adam M. Zofka, Revising thermal stresses in the TSRST for low-temperature cracking prediction, *J. Mater. Civ. Eng.* 21 (11) (2009) 680–687, [https://doi.org/10.1061/\(ASCE\)0899-1561\(2009\)21:11\(680\)](https://doi.org/10.1061/(ASCE)0899-1561(2009)21:11(680)).
- [18] D.N. Richardson, S.M. Lusher, Determination of Creep Compliance and Tensile Strength of Hot-Mix Asphalt for Wearing Courses in Missouri, 2008.
- [19] Antonio Roberto, Elena Romeo, Antonio Montepara, Riccardo Roncella, Effect of fillers and their fractional voids on fundamental fracture properties of asphalt mixtures and mastics, *Road Mater. Pavement Des.* 21 (1) (2020) 25–41, <https://doi.org/10.1080/14680629.2018.1475297>.
- [20] Rebecca S. McDaniel, Ayesha Shah, Gerald A. Huber, Audrey Copeland, Effects of reclaimed asphalt pavement content and virgin binder grade on properties of plant produced mixtures, *Asph. Paving Technol. Assoc. Asph. Paving Technol. Tech. Sess.* 13 (sup1) (2012) 161–182, <https://doi.org/10.1080/14680629.2012.657066>.
- [21] P.K. Das, Y. Tasdemir, B. Birgisso, Low temperature cracking performance of WMA with the use of the Superpave indirect tensile test, *Constr. Build. Mater.* 30 (2012) 643–649, <https://doi.org/10.1016/j.conbuildmat.2011.12.013>.
- [22] Behzad Behnia, Eshan V. Dave, Sarfraz Ahmed, William G. Buttlar, Henrique Reis, Effects of recycled asphalt pavement amounts on low-temperature cracking performance of asphalt mixtures using acoustic emissions, *Transp. Res. Res. J. Transp. Res. Board.* 2208 (1) (2011) 64–71, <https://doi.org/10.3141/2208-09>.
- [23] Brian Hill, Daniel Oldham, Behzad Behnia, Elham H. Fini, William G. Buttlar, Henrique Reis, Evaluation of low temperature viscoelastic properties and fracture behavior of bio-asphalt mixtures, *Int. J. Pavement Eng.* 19 (4) (2018) 362–369, <https://doi.org/10.1080/10298436.2016.1175563>.
- [24] Jaime Wills, Silvia Caro, Andrew Braham, Influence of material heterogeneity in the fracture of asphalt mixtures, *Int. J. Pavement Eng.* 20 (7) (2019) 747–760, <https://doi.org/10.1080/10298436.2017.1334461>.
- [25] Adam Zofka, Mihai Marasteanu, Lev Khazanovich, Iliya Yut, Comparison of data interpretation procedures for indirect tensile creep test for linear viscoelastic materials, *Road Mater. Pavement Des.* 11 (sup1) (2010) 411–441, <https://doi.org/10.1080/14680629.2010.9690340>.
- [26] M. Marastean, R. Velasquez, A.C. Falchetto, A. Zofka, Temperature creep compliance of asphalt mixtures, *IDEA Progr. Final Rep. NCHRP.* 133 (2009).
- [27] Pedro Romero, USING THE BENDING BEAM RHEOMETER FOR LOW TEMPERATURE TESTING OF Prepared For : Utah Department of Transportation Submitted By : University of Utah Authored By :, (2016).
- [28] X. Gong, P. Romero, Z. Dong, Y. Li, Investigation on the low temperature property of asphalt fine aggregate matrix and asphalt mixture including the environmental factors, *Constr. Build. Mater.* 156 (2017) 56–62, <https://doi.org/10.1016/j.conbuildmat.2017.08.142>.
- [29] F. Kaseer, A. Bajaj, A.E. Martin, E. Arámbula-Mercado, E. Hajj, Strategies for producing asphalt mixtures with high RAP content, *J. Mater. Civ. Eng.* 31 (2019) 1–16, [https://doi.org/10.1061/\(ASCE\)MT.1943-5533.0002910](https://doi.org/10.1061/(ASCE)MT.1943-5533.0002910).
- [30] A.S.M. Asib, P. Romero, F. Safazadeh, An equivalence between methods of aging for determining the low-temperature performance of hot-mix asphalt concrete mixtures containing reclaimed asphalt pavement, *Constr. Build. Mater.* 223 (2019) 198–209, <https://doi.org/10.1016/j.conbuildmat.2019.06.204>.
- [31] Jozef Judycki, A new viscoelastic method of calculation of low-temperature thermal stresses in asphalt layers of pavements, *Int. J. Pavement Eng.* 19 (1) (2018) 24–36, <https://doi.org/10.1080/10298436.2016.1149840>.
- [32] M. Wagoner, W. Buttlar, G. Paulino, P. Blankenship, Investigation of the fracture resistance of hot-mix asphalt concrete using a disk-shaped compact tension test, *Transp. Res. Rec.* 2005 (1929) 183–192, <https://doi.org/10.3141/1929-22>.
- [33] C.M. Stewart, J.G. Reyes, V.M. Garcia, Comparison of fracture test standards for a super pave dense-graded hot mix asphalt, *Eng. Fract. Mech.* 169 (2017) 262–275, <https://doi.org/10.1016/j.engfractmech.2016.10.016>.
- [34] ASTM D7313, Standard Test Method for Determining Fracture Energy of Asphalt-Aggregate Mixtures Using the Disk-Shaped Compact Tension Geometry, 2013, <https://doi.org/10.1520/D7313>.
- [35] M. Marasteanu, A. Zofka, M. Turos, X. Li, R. Velasquez, X. Li, W. Buttlar, G. Paulino, A. Braham, E. Dave, Investigation of low temperature cracking in asphalt pavements national pooled fund study 776, (2007).
- [36] W. Buttlar, J. Meister, B. Jahangiri, H. Majidifard, P. Rath, Performance Characteristics of Modern Recycled Asphalt Mixes in Missouri, Including

- Ground Tire Rubber, Recycled Roofing Shingles, and Rejuvenators, 2019. <https://orcid.org/0000-0002-1545-0165>.
- [37] W. Buttlar, B. Jahangiri, P. Rath, H. Majidifard, L. Urrea, J. Meister, H. Brown, Development of a Performance-Related Asphalt Mix Design Specification for the Illinois Tollway, n.d.
- [38] William G. Buttlar, Brian C. Hill, He Wang, Walaa Mogawer, Performance space diagram for the evaluation of high- and low-temperature asphalt mixture performance, *Road Mater. Pavement Des.* 18 (sup1) (2017) 336–358, <https://doi.org/10.1080/14680629.2016.1267446>.
- [39] Behnam Jahangiri, Hamed Majidifard, James Meister, William G. Buttlar, Performance evaluation of asphalt mixtures with reclaimed asphalt pavement and recycled asphalt shingles in missouri, *Transp. Res. Rec.* 2673 (2) (2019) 392–403, <https://doi.org/10.1177/0361198119825638>.
- [40] P. Rath, J.E. Love, W.G. Buttlar, H. Reis, Performance analysis of asphalt mixtures modified with ground tire rubber modifiers and recycled materials, *Sustain.* 11 (2019) 1792, <https://doi.org/10.3390/su11061792>.
- [41] A.F. Braham, W.G. Buttlar, T.R. Clyne, M.O. Marasteanu, M.I. Turos, The effect of long-term laboratory aging on asphalt concrete fracture energy, *J. Assoc. Asph. Paving Technol.* 78 (2009).
- [42] W. Flügge, *Viscoelasticity* - 2nd revised edition, 1975. <https://doi.org/10.1007/978-3-662-02276-4>.
- [43] Lev Khazanovich, The elastic-viscoelastic correspondence principle for non-homogeneous materials with time translation non-invariant properties, *Int. J. Solids Struct.* 45 (17) (2008) 4739–4747, <https://doi.org/10.1016/j.ijsolstr.2008.04.011>.
- [44] G. Wijk, Some new theoretical aspects of indirect measurements of the tensile strength of rocks, *Int. J. Rock Mech. Min. Sci. Geomech. Abstr.* 15 (1978) 124, [https://doi.org/10.1016/0148-9062\(78\)91493-6](https://doi.org/10.1016/0148-9062(78)91493-6).
- [45] Eshan V. Dave, Glaucio H. Paulino, William G. Buttlar, Viscoelastic Functionally Graded Finite-Element Method Using Correspondence Principle, *J. Mater. Civ. Eng.* 23 (1) (2011) 39–48, [https://doi.org/10.1061/\(ASCE\)MT.1943-5533.0000006](https://doi.org/10.1061/(ASCE)MT.1943-5533.0000006).
- [46] A. User, S. Reference, *Abaqus User Subroutines Reference Manual*, (n.d.).